

QISTA-NET: DNN ARCHITECTURE TO SOLVE ℓ_q -NORM MINIMIZATION PROBLEM AND IMAGE COMPRESSED SENSING

Gang-Xuan Lin, Shih-Wei Hu, and Chun-Shien Lu

Institute of Information Science, Academia Sinica, Taipei, Taiwan

ABSTRACT

In this paper, we reformulate the non-convex ℓ_q -norm minimization problem with $q \in (0, 1)$ into a 2-step problem, which consists of one convex and one non-convex subproblems, and propose a novel iterative algorithm called QISTA (ℓ_q -ISTA) to solve the (ℓ_q) -problem. By taking advantage of deep learning in accelerating optimization algorithms, together with the speedup strategy that using the momentum from all previous layers in the network, we propose a learning-based method, called QISTA-Net-s, to solve the sparse signal reconstruction problem. Extensive experimental comparisons demonstrate that the QISTA-Net-s yield better reconstruction qualities than state-of-the-art ℓ_1 -norm optimization (plus learning) algorithms even if the original sparse signal is noisy. On the other hand, based on the network architecture associated with QISTA, with considering the use of convolution layers, we proposed the QISTA-Net-n for solving the image CS problem, and the performance of the reconstruction still outperforms most of the state-of-the-art natural images reconstruction methods. QISTA-Net-n is designed in unfolding QISTA and adding the convolutional operator as the dictionary. This makes QISTA-Net-s interpretable. We provide complete experimental results that QISTA-Net-s and QISTA-Net-n contribute the better reconstruction performance than the competing.

Index Terms— Compressed sensing, ℓ_q -norm regularization problem, Non-convex optimization, Convolution neural network

1. INTRODUCTION

1.1. Background and Problem Definition

In sparse signal recovery like compressive sensing (CS) [1, 2], we usually let $x_0 \in \mathbb{R}^n$ denote a k -sparse signal to be sensed, let $A \in \mathbb{R}^{m \times n}$ represent a sampling matrix, and let $y \in \mathbb{R}^m$ be the measurement vector defined as

$$y = Ax_0, \quad (1)$$

where $k < m < n$ and $0 < \frac{m}{n} < 1$ is defined as the measurement rate. At the decoder, x_0 can be recovered based on its

sparsity by means of solving ℓ_0 -norm regularization problem:

$$(\ell_0) \quad \min_x \frac{1}{2} \|y - Ax\|_2^2 + \lambda \|x\|_0, \quad (2)$$

where $\lambda > 0$ is a regularization parameter.

The (ℓ_0) -problem is NP-hard [3] as it suffers from the non-convexity and discontinuity of objective function so that there is no efficient algorithm to solve its global minima. An effective way to recover the original sparse signal x_0 is relaxing the objective function in (2) as the ℓ_1 -norm regularization problem, which is known as ‘‘LASSO’’ [4, 5]:

$$(\text{LASSO}) \quad \min_x \frac{1}{2} \|y - Ax\|_2^2 + \lambda \|x\|_1. \quad (3)$$

Nevertheless, considering LASSO cannot recover the original sparse signal under low measurement rates (say $m < 3k$) [6], ℓ_q -norm regularization is suggested [6, 7]. The (non-convex) ℓ_q -norm regularization problem has the form

$$(\ell_q) : \quad \min_x \frac{1}{2} \|y - Ax\|_2^2 + \lambda \|x\|_q^q, \quad (4)$$

where $0 < q < 1$, and $\|x\|_q = \sum_{i=1}^n (|x_i|^q)^{1/q}$ is the ℓ_q -quasi-norm (which is usually called ℓ_q -norm). In comparison with (ℓ_0) -problem and LASSO, the authors concluded that decreasing q further decreases the required measurement rate and by less and less as q gets smaller [6, 7].

It is noted that the discussions regarding (ℓ_q) -problem or effective algorithms in finding its optimal solution are very rare in the literature. Furthermore, (ℓ_q) -problem is also NP-hard [8], and literature review reveals that solving (ℓ_q) -problem suffers from non-convexity, leading to a local-non-global optimal solution. Although it is difficult to find the global optimal solution, under good initial iterative point, the limit point gained by iterative algorithms converging to a local-non-global optimal solution is still closer to $x_{\ell_0}^*$ of (ℓ_0) -problem than $x_{\ell_1}^*$ of LASSO [9], where x^* is the global optimal solution.

1.2. Related Works

Traditionally, one always approximates the optimal solution to (ℓ_0) -problem and LASSO, by employing proximal gra-

gradient descent method (PGD), which is also known as iterative hard-threshold algorithm (IHT) [10] and iterative soft-threshold algorithm (ISTA) [5]. However, IHT could obtain better reconstruction quality than ISTA only if the original signal is very sparse ($k/n < 5\%$) and/or measurement rate is high ($m/n > 50\%$) [11, 12]. The use of PGD to solve (ℓ_q) -problem is not popular because there is no closed-form solution to proximal operator associated with its regularization term [11]. Beck and Teboulle speed up ISTA by using Nesterov’s acceleration method (insert momentum after gradient descent step), which is known as FISTA [13], whereas Donoho *et al.* consider an efficient algorithm called AMP (approximate message passing) that incorporates ISTA with Onsager term in measurement residue $y - Ax^t$ [14].

On the other hand, in solving the (ℓ_q) -problem, Cui *et al.* [15] propose to utilize the iterative thresholding (IT) algorithm in finding the global optimal solution of surrogate function. Xu *et al.* [12] design a half thresholding algorithm by thresholding representation theory to solve the (ℓ_q) -problem when $q = 1/2$. Cao *et al.* [16] deduce the thresholding formula in [12] to derive the extension thresholding formula, which can solve the (ℓ_q) -problem when $q = 2/3$. However, most of the algorithms still suffer from the non-convexity of ℓ_q -regularized term, leading to a local-non-global optimal solution, though such a solution results in better reconstruct performance than IHT and ISTA, which solve (ℓ_0) -problem and LASSO, respectively. Moreover, [12] and [16] restrict the choice of q ($= 1/2$ or $= 2/3$) and the other aforementioned methods have to tune an appropriate q to get better results, which violates the fact that q should be small [6].

Recently, compare with the traditional iterative methods, deep learning-based paradigm has received considerable attention due to its extremely low complexity and outstanding performance. By incorporating deep learning models and optimization methods, several deep network-based sparse signal reconstruction methods have been proposed in the literature.

To accelerate the sparse 1D signal reconstruction methods, in 2010, Gregor and LeCun [17] proposed a learned ISTA method, called LISTA. Borgerding *et al.* [18] proposed a learned AMP method, called LAMP. Based on the theoretical linear convergence of LISTA, Chen *et al.* [19] introduced the necessary conditions for the LISTA, and proposed the LISTA-CP, LISTA-SS, and LISTA-CPSS to improve reconstruction performance with fewer training parameters. In order to speed up the training process, Ito *et al.* [20] proposed the so-called TISTA (trainable ISTA) method, which only needs $T + 2$ training parameters and has high reconstruction performance, where T is the layer number.

In the reconstruction of natural images, Mousavi *et al.* [21] first proposed to apply a stacked denoising auto-encoder (SDA) to learn the representation and to reconstruct natural images from their CS measurements. Kulkarni *et al.* [22] further developed a CNN-based method, dubbed ReconNet, to reconstruct the natural images. To the best of our knowl-

edge, ReconNet probably the first one who solves image CS problem by CNN-based method. Similar to [22], all of the network architectures in MS-CSNet [23], DR²-Net [24], MSRNet [25], CSNet⁺ [26], and SCSNet [27] are heuristic designs in solving CS. Another category aims to develop learning-based methods designed based on an iterative-based algorithm. The methods [28] [29] unfolded the parameters of the iterative-based algorithm, within the framework of CNN to design the network architectures.

1.3. Contributions

1. We reformulate (ℓ_q) -norm minimization problem into 2-step problem that transfers the difficulty coming from non-convexity to another non-convex optimization problem that can be trivially solved. Then we design an algorithm called QISTA that approximates the optimal solution of (ℓ_q) -problem precisely.
2. QISTA-Net-s is a DNN architecture by unfolding specific parameters in QISTA to accelerate the reconstruction. After unfolding, we utilize the momentum coming from all previous layers to further speed up the network architecture. The use of momentum for network architecture is novel in literature.
3. The performance of QISTA-Net-s in reconstruct the sparse signal is better than state-of-the-art ℓ_1 -norm learning-based methods, even in noisy environments.
4. In reconstructing the natural images, the proposed method QISTA-Net-n is comparable with state-of-the-art learning-based methods, including the method that specially designed for reconstructing the natural image.

1.4. Organization of This Paper

The remainder of this paper is organized as follows. In Sec. 2, we propose an iterative method, called QISTA, to solve the (ℓ_q) -problem (4). Based on QISTA, we propose a learning-based method, called QISTA-Net-s, in solving problem (4) in Sec. 3. Again, based on QISTA, we propose a learning-based method in solving the image CS problem in Sec. 4. The comparison with the state-of-the-art methods of QISTA, QISTA-Net-s, and QISTA-Net-n are provided in Sec. 5, Sec. 6, and Sec. 7, respectively.

2. ITERATIVE METHOD FOR SOLVING THE SPARSE SIGNAL RECONSTRUCTION PROBLEM: QISTA

In Sec. 2.1, we first approximate the (ℓ_q) -problem (4) and reformulate it into the 2-step problem. We then propose an iterative algorithm, QISTA, for solving the (ℓ_q) -problem in Sec. 2.2. The insight of QISTA is described in Sec. 2.3.

2.1. Reformulate (ℓ_q) -problem as 2-Step Problem

To solve (ℓ_q) -problem, it is first approximated as

$$\min_x F(x) = \frac{1}{2} \|y - Ax\|_2^2 + \lambda \sum_{i=1}^n \frac{|x_i|}{(|x_i| + \varepsilon_i)^{1-q}}, \quad (5)$$

where $\varepsilon_i > 0$ for all $i \in [1 : n]$. We can see that the objective function in (5) is equivalent to the one in (4) provided $\varepsilon_i = 0$ for all i , i.e.,

$$\lim_{\varepsilon_i \rightarrow 0^+} \frac{|x_i|}{(|x_i| + \varepsilon_i)^{1-q}} = |x_i|^q.$$

This means the problem (5) approximates to the (ℓ_q) -problem (4) well if ε_i 's are small enough.

Second, we extend $F(x)$ in the problem (5) into high-dimensional functional $H(x, c)$, then relax the problem (5) (in the sense of feasible set from \mathbb{R}^n to $\mathbb{R}^n \times \mathbb{R}^n$) into

$$\min_{x,c} H(x, c) = \frac{1}{2} \|y - Ax\|_2^2 + \lambda \sum_{i=1}^n \frac{|x_i|}{(|c_i| + \varepsilon_i)^{1-q}}. \quad (6)$$

We can see that the functional $H(x, c)$ degenerates to $F(x)$ if $c = x$. Thus, we can reformulate the problem (5) as a 2-step problem:

$$\begin{cases} \min_x H(x, \bar{c}) = \frac{1}{2} \|y - Ax\|_2^2 + \lambda \sum_{i=1}^n \frac{|x_i|}{(|\bar{c}_i| + \varepsilon_i)^{1-q}}, \\ \min_c |H(\bar{x}, c) - H(\bar{x}, \bar{x})|, \end{cases} \quad (7)$$

where \bar{x} and \bar{c} are optimal solutions to the first problem (called x -subproblem) and the second problem (called c -subproblem), respectively.

Theorem 2.1. *If (x^*, c^*) is an optimal solution pair to 2-step problem (7), then x^* is an optimal solution to problem (5), and vice versa.*

Proof. Let (x^*, c^*) be an optimal solution pair to (7), since the optimal value of c -subproblem is obviously 0, we have $H(x^*, c^*) = H(x^*, x^*)$, which equals to $F(x^*)$ (because $H(x, x) = F(x)$), therefore x^* is an optimal solution to (5).

On the other hand, let x^* be an optimal solution to (5), then $c^* = x^*$ is an optimal solution to c -subproblem of (7), whereas x -subproblem is exactly equivalent to (5). ■

We can see that the c -subproblem has global minimum solution

$$\bar{c} = \bar{x}, \quad (8)$$

whereas the x -subproblem is in a weighted-LASSO form

$$\min_x \frac{1}{2} \|y - Ax\|_2^2 + \lambda \sum_{i=1}^n |w_i x_i|, \quad (9)$$

(the weight of $|x_i|$ is $\frac{\lambda}{(|\bar{c}_i| + \varepsilon_i)^{1-q}}$), and thus the x -subproblem can be solved iteratively by proximal gradient descent algorithm [30] as

$$\begin{cases} r^t = x^t + \beta A^T (y - Ax^t) \\ x^{t+1} = \eta(r^t; \theta), \end{cases} \quad (10)$$

where $\theta_i = \frac{\lambda}{(|\bar{c}_i| + \varepsilon_i)^{1-q}}, \forall i$, (when we solve the x -subproblem, \bar{c} is a given constant vector, so θ is fixed in each iteration) $\eta(\cdot; \cdot)$ is component-wise soft-thresholding operator

$$\eta(x; \theta) = \text{sign}(x) \cdot \max\{0, |x| - \theta\}.$$

The iterative process in Eq. (10) consists of two steps, i.e., gradient descent step followed by truncation step.

2.2. QISTA

In Eq. (10), the iterative process is formed by the alternating iteration of two points: r^t and x^t . In the first step (gradient descent step) of Eq. (10), the step size β is always chosen from $(0, \frac{1}{L_f}]$ [5, 13, 18], where $f(x) = \frac{1}{2} \|y - Ax\|_2^2$ and L_f is the smallest Lipschitz constant of $\nabla f(x)$. Indeed $L_f = \|A\|_2^2$, where $\|A\|_2$ is the spectral norm of A . We can see that $r^t - x^t = \beta A^T (y - Ax^t)$, which implies

$$\begin{aligned} \|r^t - x^t\|_2^2 &= \beta \|A^T (y - Ax^t)\|_2^2 \\ &\leq \beta \|A^T\|_2^2 \|y - Ax^t\|_2^2 \\ &= \beta \|A\|_2^2 \|y - Ax^t\|_2^2 \\ &\leq \|y - Ax^t\|_2^2. \end{aligned}$$

Since the x -subproblem is convex, the proximal gradient descent algorithm (10) is global-convergence [13], then we have $\lim_{t \rightarrow \infty} x^t = \bar{x}$, and

$$\lim_{t \rightarrow \infty} \|r^t - x^t\|_2 \leq \|y - A\bar{x}\|_2. \quad (11)$$

On the other hand, if the penalty coefficient λ of x -subproblem in 2-step problem (7) is small enough, the magnitude of the regularization term $(\lambda \sum_{i=1}^n \frac{|x_i|}{(|\bar{c}_i| + \varepsilon_i)^{1-q}}$, the penalty term) is small relative to the magnitude of the term $f(x) = \frac{1}{2} \|y - Ax\|_2^2$. This means that the optimal solution \bar{x} to x -subproblem leads to a relatively small value $\frac{1}{2} \|y - A\bar{x}\|_2^2$. This is to say, if λ is small enough, by Eq. (11), we have

$$\lim_{t \rightarrow \infty} r^t \approx \lim_{t \rightarrow \infty} x^t = \bar{x}. \quad (12)$$

In other words, the two points r^t and x^t are close if t is large enough, $\beta \in (0, \frac{1}{L_f}]$, and λ is small enough. Under the circumstance, instead of choosing Eq. 8 as the solution of the c -subproblem in Eq. 7, the approximation

$$\bar{c} \approx r^t, \quad (13)$$

where r^t is the iterative point of the proximal gradient descent algorithm that solves the x -subproblem, was adopted. The benefits of using the approximate optimal solution instead of the exact optimal solution for c -subproblem, will be discussed in Sec. 2.3.

At last, we summarized the alternative iteration for solving the 2-step problem (7) as follows:

$$\begin{cases} r^t = x^{t-1} + \beta A^T (y - Ax^{t-1}), \\ c^t = r^t, \\ x_i^t = \eta \left(r_i^t; \frac{\lambda}{(|c_i^t| + \varepsilon_i)^{1-q}} \right), \forall i \end{cases} \quad (14)$$

which is equivalent to

$$\text{(QISTA)} : \begin{cases} r^t = x^{t-1} + \beta A^T (y - Ax^{t-1}), \\ x_i^t = \eta \left(r_i^t; \frac{\lambda}{(|r_i^t| + \varepsilon_i)^{1-q}} \right), \forall i. \end{cases} \quad (15)$$

We name it QISTA (ℓ_q -ISTA).

Algorithm 1 QISTA

- 1: Set parameters $\beta, \lambda, \text{TOL}$;
 - 2: Initial $x^{\text{init}} = x^0 = x^{-1} \in \mathbb{R}^n$;
 - 3: **repeat**
 - 4: $r^t = x^{t-1} + \beta A^T (y - Ax^{t-1})$;
 - 5: $x_i^t = \eta \left(r_i^t; \frac{\lambda}{(|r_i^t| + \varepsilon_i)^{1-q}} \right), \forall i \in [1 : n]$;
 - 6: **until** ($\|x^t - x^{t-1}\|_2 < \text{TOL}$)
-

2.3. Insight of QISTA

The iterative process in Algorithm 1 consists of two steps, *i.e.*, the gradient descent step (step 4), followed by the truncation step (step 5). The gradient descent step updates the point by moving the current iterative point x^{t-1} , along the direction $A^T (y - Ax^{t-1})$ which perpendicular to the null space of A , with the step size β , to the updated point r^t (as shown in Fig. 1, moving the green point x^{t-1} to the blue point r^t). In the truncation step, the truncated parameter

$$\theta_{r^t}(i) = \frac{\lambda}{(|r_i^t| + \varepsilon_i)^{1-q}}$$

is determined by $|r_i^t|$ (λ, ε_i , and q are constants). This says that if $|r_i^t|$ is non-zero, or larger than the other components $|r_j^t|$ (which we guess that the index i may in the support set of x_0), then $\theta_{r^t}(i)$ is relatively small. Conversely, if $|r_i^t|$ is zero, or is a relatively small number (which we guess that the i^{th} component of x_0 is zero), then $\theta_{r^t}(i)$ is relatively large.

The input of the truncation step, r^t , is truncated by θ_{r^t} , componentwise. We can see that if $|r_i^t|$ is a large number,

the $\theta_{r^t}(i)$ is almost zero, and then the truncate operator $\eta(r_i^t; \theta_{r^t}(i))$ will preserve the value of r_i^t . Conversely, if $|r_i^t|$ is a small number, the truncate operator $\eta(r_i^t; \theta_{r^t}(i))$ will decrease the value of $|r_i^t|$. As shown in Fig. 1, the truncation step in QISTA updates the point r^t (blue points) by moving it, along the direction perpendicular to the set $\{x : \|x\|_q = \|r^t\|_q\}$ (is a contour line $\{x : \|x\|_q = s\}$ for some constant s) approximately, to the point x^t (green points). As the iteration progresses, the $x^t = \eta(r^t; \theta_{r^t})$ will gradually approach the optimal solution to (ℓ_q)-problem. Remark that the truncate parameter θ_{r^t} adapts to the value of r^t , componentwise, instead of applying the same truncation value to every component, as of ISTA. This indicates why QISTA is better than ISTA.

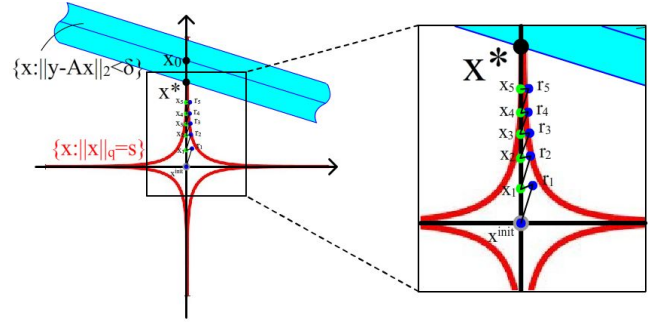


Fig. 1: The iterative process of QISTA. The water-colored region is the set $\{x : \|y - Ax\|_2 < \delta\}$, where δ is a constant related to λ . The red line is the contour line $\{x : \|x\|_q = s\}$ for a constant s . x_0 is the ground-truth, whereas x^* is the optimal solution to (ℓ_q)-problem.

2.4. Remarks

Basically, in QISTA, we first approximate the (ℓ_q)-problem by (5), and then reformulate it into the 2-step problem (7). Since the objective function $F(x)$ in (5) is non-convex, it is difficult to attain the global minima; whereas the functional $H(x, c)$ in (7) is convex in x for any given c , but non-convex in c for any given x . However, since the x -subproblem is convex, the proximal gradient descent algorithm (10) to find its optimal solution is global-convergence under mild parameter setting [13]. On the other hand, although the c -subproblem is non-convex, the non-convexity can be avoided because there is a trivial global minimum solution, *i.e.*, $\bar{c} = \bar{x}$.

3. LEARNING-BASED METHOD FOR SOLVING THE SPARSE SIGNAL RECONSTRUCTION PROBLEM: QISTA-NET-S

Similar to [17, 18, 19], to accelerate QISTA, we design a deep neural network (DNN) architecture by unfolding the parameters βA^T , λ , and ε , into \mathcal{A}^t , λ^t , and \mathcal{E}^t , respectively. The network architecture then has the form

$$\begin{cases} r^t = x^{t-1} + \mathcal{A}^t (y - Ax^{t-1}), \\ x_i^t = \eta \left(r_i^t; \frac{\lambda^t}{(|r_i^t| + \mathcal{E}_i^t)^{1-q}} \right), \forall i \in [1 : n], \end{cases} \quad (16)$$

where t stands for the t^{th} layer of the network.

The insight of (16) is that, the first equation is corresponding to the gradient descent step, by letting βA^T be a training parameter, the NN architecture is trying to modify the descent direction and find the appropriate step size simultaneously. Besides, λ^t in the second equation is to learn the appropriate truncated rate with respect to the current iterative point r^t ; and, \mathcal{E}^t is to control the similarity between approximated (ℓ_q) -problem (5) and the original (ℓ_q) -problem (4).

In FISTA [13], the gradient descent step considers the previous iterative direction called momentum. And, in AMP [14], the residue in the measurement domain considers the previous iterative residue called the Onsager term. Inspired by FISTA and AMP, we further accelerate the network in (16) by adding the ‘‘momentum’’ that coming from the descent direction of all previous layers with an appropriate weight. The resultant is shown in Algorithm 2, which is called QISTA-Net-s (QISTA in Network model for Sparse signal reconstruction).

Algorithm 2 QISTA-Net-s

- 1: **for** $t = 1$ to T **do**
 - 2: $D^t = \mathcal{A}^t (y - Ax^{t-1})$;
 - 3: $r^t = x^{t-1} + \sum_{j=1}^t D^j$;
 - 4: $D^j = \frac{\gamma}{m} \cdot D^j, \forall j \in [1 : t]$;
 - 5: $x_i^t = \eta \left(r_i^t; \frac{\lambda^t}{(|r_i^t| + \mathcal{E}_i^t)^{1-q}} \right), \forall i \in [1 : n]$;
 - 6: **end for**
-

The learning parameters in Algorithm 2 are $\{\mathcal{A}^t, \lambda^t, \mathcal{E}^t\}_{t=1}^T$, and the loss function is the MSE-loss:

$$\mathcal{L}_{\text{MSE}} = \frac{1}{n} \|x_0 - x^T\|_2^2. \quad (17)$$

where x^T is the output of the algorithm.

In Algorithm 2, D^t in Step 2 is the descent direction of the current layer t , $\sum_{j=1}^{t-1} D^j$ in Step 3 is the momentum consisting of the descent direction of previous layers, and Step 4 controls the effect of momentum appropriately. However, unlike the acceleration of traditional iterative methods such as FISTA [13], the improvement effect in QISTA-Net-s can

only draw empirical conclusions without being able to conduct mathematical analysis.

Remark that the first equation in (16) is corresponding to the gradient descent step (as in Step 4 of Algorithm 1), which unfold both A and βA^T to be learning parameters is commonly adopted in LISTA [17], LAMP [18], and other learning-based methods. According to Theorem 1 in [19], we only set βA^T to be a learning parameter and keep A as the original matrix to reduce the training time without loss of reconstruction performance.

4. LEARNING-BASED METHOD FOR RECONSTRUCTING THE NATURAL IMAGES: QISTA-NET-N

In Sec. 3, we proposed the QISTA-Net-s for the sparse 1D signal reconstruction problem. Here we address the other critical issue called natural image reconstruction problem.

In this section, we consider the natural image $X_0 \in \mathbb{R}^{n_1 \times n_2}$, where $n_1 \times n_2$ is image size, and its vector representation $x_0 \in \mathbb{R}^n$, where $n = n_1 \cdot n_2$. The natural image is, in general, a non-sparse signal, and it always exists a sparse representation in a specific domain. The traditional optimization method usually reconstruct the original image x_0 by solving the following ℓ_1 -norm regularization problem in LASSO form:

$$\min_x \frac{1}{2} \|y - Ax\|_2^2 + \lambda \|\Psi x\|_1, \quad (18)$$

where $A \in \mathbb{R}^{m \times n}$ is the sensing matrix, and $\Psi \in \mathbb{R}^{n \times n}$ is dictionary that represent x_0 in sparse coefficient with respect to the specific domain. In this section, we consider the ℓ_q -norm regularization problem in the form:

$$\min_x \frac{1}{2} \|y - Ax\|_2^2 + \lambda \|\Psi x\|_q^q, \quad (19)$$

where $0 < q < 1$.

Similar to the process from Eq. (5) to Eq. (7) in Sec. 2.1, we can reformulate the problem (19) as a 2-step problem:

$$\begin{cases} \min_x H(x, \bar{c}) = \frac{1}{2} \|y - Ax\|_2^2 + \lambda \sum_{i=1}^n \frac{|(\Psi x)_i|}{(|\bar{c}_i| + \varepsilon_i)^{1-q}}, \\ \min_c |H(\bar{x}, c) - H(\bar{x}, \Psi \bar{x})|, \end{cases} \quad (20)$$

where $\varepsilon_i > 0$ for all $i \in [1 : n]$, and \bar{x} and \bar{c} are optimal solutions to the x -subproblem and the c -subproblem, respectively.

4.1. Generalized proximal operator

In this subsection, we aim to design an explicit iterative process that solves the x -subproblem in (20). In the x -subproblem, we can see that the regularization term of the objective function is in the form of the composite function $\|\Psi(x)\|_{1,w} = \left(\|\cdot\|_{1,w} \circ \Psi \right)(x)$, where $\|x\|_{1,w} =$

$\sum_{i=1}^n w_i |x_i|$ with $w_i = \frac{\lambda}{(|\bar{c}_i| + \varepsilon_i)^{1-q}}$. Therefore the proximal gradient descent algorithm [30] for solving the x -subproblem has the form

$$\begin{cases} r^t = x^{t-1} + \beta A^T (y - Ax^{t-1}), \\ x^t = \text{prox}_{\|\Psi(\cdot)\|_{1,w}}(r^t). \end{cases} \quad (21)$$

Different from the problem (9), there is no useful calculus rule for computing the proximal operator of a composite function $\|\Psi(\cdot)\|_{1,w}$ so that Eqs. (21) cannot be explicitly written as the iterative process similar to Eqs. (10). To address the circumstance, we introduce the generalized proximal operator by the following theorem:

Theorem 4.1. [30] *Let $g : \mathbb{R}^n \rightarrow (-\infty, \infty]$ be a proper closed convex function, and let $f(x) = g(\mathcal{A}(x) + b)$, where $b \in \mathbb{R}^n$ and $\mathcal{A} : \mathbb{R}^{\hat{n}} \rightarrow \mathbb{R}^n$ is a linear transformation satisfying $\mathcal{A} \circ \mathcal{A}^T = \gamma \cdot I_n$ for some constant $\gamma > 0$. Then for any $x \in \mathbb{R}^{\hat{n}}$,*

$$\text{prox}_f(x) = x + \frac{1}{\gamma} \mathcal{A}^T (\text{prox}_{\gamma g}(\mathcal{A}(x) + b) - (\mathcal{A}(x) + b)).$$

As described in theorem 4.1, we can see that if the dictionary Ψ is linear and satisfies a certain orthogonality condition, the solution to the proximal operator of the regularized term $\lambda \sum_{i=1}^n \frac{|\langle \Psi x, e_i \rangle|}{(|\bar{c}_i| + \varepsilon_i)^{1-q}}$ in x -subproblem can be found.

After replacing $g(x)$ and $\mathcal{A}(x)$ in Theorem 4.1 by $\|\cdot\|_{1,w}$ and $\Psi(x)$, respectively, the solution to the proximal operator in Eq. (21) becomes

$$\begin{aligned} & \text{prox}_{\|\Psi(\cdot)\|_{1,w}}(r^t) \\ &= r^t + \frac{1}{\gamma_c} \Psi^T (\eta(\Psi(r^t); \gamma_c) - \Psi(r^t)), \end{aligned} \quad (22)$$

where $\gamma_c = \frac{\lambda}{(|\bar{c}| + \varepsilon)^{1-q}}$, and we call Eq. (22) a generalized proximal operator.

Similar to Eq. (10), the proximal gradient descent algorithm for solving x -subproblem in (20) can be written in the iterative process as

$$\begin{cases} r^t = x^{t-1} + \beta A^T (y - Ax^{t-1}) \\ x^t = r^t + \frac{1}{\gamma_c} \Psi^T (\eta(\Psi(r^t); \gamma_c) - \Psi(r^t)). \end{cases} \quad (23)$$

On the other hand, Ψ in problem (19) plays the role of a dictionary that, in general, represent the non-sparse signal as a sparse coefficient with respect to the specific domain. However, the classic fixed domain (e.g. DCT, DFT, wavelet, gradient domain, etc.) usually result in poor reconstruction performance. Besides, Ψ is generally treated to be an over-complete dictionary (i.e., $\Psi \in \mathbb{R}^{N \times n}$ with $N > n$) to seek better performance.

However, as $N > n$, the assumption $\Psi \circ \Psi^T = \gamma_c I_N$ in Theorem 4.1 is not satisfied at all. Thus, it is required to choose a Ψ^\dagger that satisfies $\Psi \circ \Psi^\dagger \approx \gamma_c I_N$. We can see that the

left inverse of Ψ always exists, i.e., $\tilde{\Psi} = (\Psi^T \circ \Psi)^{-1} \circ \Psi^T$ satisfy $\tilde{\Psi} \circ \Psi = I_n$, due to the fact that $N > n$. Then we have

$$\begin{aligned} \Psi^\dagger &= I_n \circ \Psi^\dagger \\ &= (\tilde{\Psi} \circ \Psi) \circ \Psi^\dagger \\ &= \tilde{\Psi} \circ (\Psi \circ \Psi^\dagger) \\ &\approx \tilde{\Psi} \circ \gamma_c I_N \\ &= \gamma_c \tilde{\Psi}. \end{aligned} \quad (24)$$

Therefore, the assumption in Theorem 4.1 can be relaxed as $\Psi^T = \bar{\gamma} \tilde{\Psi}$, where $\bar{\gamma}$ is a constant. Thus, the solution to the proximal operator in Eq. (21) can be approximated as

$$x^t = r^t + \bar{\gamma} \tilde{\Psi} (\eta(\Psi(r^t); \gamma_c) - \Psi(r^t)). \quad (25)$$

4.2. Convolutional Dictionary

Inspired by the representation power of CNN [31] and its universal approximation property [32], and the approach to sparsify natural images in [28], the dictionary Ψ is adopted in the form as

$$\Psi = \mathcal{C}_3 (\text{ReLU}(\mathcal{C}_2 (\text{ReLU}(\mathcal{C}_1(x))))), \quad (26)$$

where $\mathcal{C}_1, \mathcal{C}_2$, and \mathcal{C}_3 are convolution operators, and ReLU is a rectified linear unit, and we call this form as a convolutional dictionary.

On the other hand, to exhibit a ‘‘left-inverse’’ structure of Ψ , $\tilde{\Psi}$ is also adopted in the form of the convolutional dictionary as

$$\tilde{\Psi} = \mathcal{C}_6 (\text{ReLU}(\mathcal{C}_5 (\text{ReLU}(\mathcal{C}_4(x))))), \quad (27)$$

where $\mathcal{C}_4, \mathcal{C}_5$, and \mathcal{C}_6 are convolution operators. Based on the relaxation that $\Psi^T = \bar{\gamma} \tilde{\Psi}$, we present a suitable loss function appropriately to ensure the left-inverse relation between Ψ and $\tilde{\Psi}$. The loss function will be described in Sec. 4.4.

4.3. QISTA-Net-n

After determining the dictionaries, the iterative process (23) becomes:

$$\begin{cases} r^t = x^{t-1} + \beta A^T (y - Ax^{t-1}) \\ x^t = r^t + \bar{\gamma} \tilde{\Psi} (\eta(\Psi(r^t); \gamma_c) - \Psi(r^t)), \end{cases} \quad (28)$$

where Ψ and $\tilde{\Psi}$ are as shown in Eqs. (26) and (27).

Since Eq. (28) is the iterative process that solves the x -subproblem in 2-step problem (20), and, similar to Sec. 2.2, we also approximate the solution to the c -subproblem by $\bar{c} \approx \Psi(r^t)$ (as in Eq. (13)) instead of $\Psi(x^t)$. Therefore, similar to Eq. (14) and Eq. (15), we also propose an iterative process that solves the 2-step problem (20) as

$$\begin{cases} r^t = x^{t-1} + \beta A^T (y - Ax^{t-1}) \\ x^t = r^t + \bar{\gamma} \tilde{\Psi} (\eta(\Psi(r^t); \gamma_r) - \Psi(r^t)), \end{cases} \quad (29)$$

where $\gamma_r = \frac{\lambda}{(|\Psi(r^t)| + \varepsilon)^{1-q}}$.

Similar in Sec. 3, we design a DNN architecture by unfolding the parameters β , A^T , A , $\bar{\gamma}$, $\tilde{\Psi}$, Ψ , and λ , into β^t , \mathcal{B} , \mathcal{A} , α^t , $\tilde{\Psi}^t$, Ψ^t , and λ^t , respectively. The network architecture then has the form

$$\begin{cases} r^t = x^{t-1} + \beta^t \mathcal{B} (y - \mathcal{A}x^{t-1}) \\ x^t = r^t + \alpha^t \tilde{\Psi}^t (\eta(\Psi^t(r^t); \gamma_r^t) - \Psi^t(r^t)), \end{cases} \quad (30)$$

where $\gamma_r^t = \frac{\lambda^t}{(|\Psi^t(r^t)| + \varepsilon)^{1-q}}$.

Remark that the fully connected (FC) layers \mathcal{B} and \mathcal{A} are common used in every layers, and the other training parameters are trained independently with respect to the layer. Besides, the structures of $\tilde{\Psi}^t$ and Ψ^t are as shown in Eqs. (26) and (27), therefore the training parameters is indeed the convolution operators \mathcal{C}_i , $i = 1, 2, \dots, 6$.

In (30), the first step consists of matrix and vector multiplications and affine transformations, that is, the calculation in the first step is affine-linear, and the current iterative point is in the time domain. However, the second step consists of non-linear operators ReLU, and convolution operators. Specifically, the input r^t of this step is in the time domain, whereas we hope the convolutional operator Ψ^t , which play the role of the dictionary, transform r^t into a specific domain which should represent r^t as a sparse vector. Therefore, before the Ψ^t act on r^t , we consider an extra convolution operator to transform the r^t in the time domain into the convolution domain, to helping Ψ^t more easily to learn a good sparse representation dictionary. That is, we act the convolution operator \mathcal{C}_0^t before the Ψ^t , then $\Psi^t(r^t)$ in Eq. (30) becomes

$$\Psi^t(r^t) \leftarrow \Psi^t(\mathcal{C}_0^t(r^t)).$$

Also, after the $\tilde{\Psi}^t$ operated, we also consider an extra convolution operator \mathcal{C}_7^t to transform the $\tilde{\Psi}^t(s^t)$, where $s^t = \eta(\Psi^t(r^t); \gamma^t) - \Psi^t(r^t)$, in the specific domain back into the time domain. That is, $\tilde{\Psi}^t(s^t)$ becomes

$$\tilde{\Psi}^t(s^t) \leftarrow \mathcal{C}_7^t(\tilde{\Psi}^t(s^t)).$$

With the extra convolution transformations, the training parameters

$$\{\beta^t, \mathcal{B}, \mathcal{A}, \alpha^t, \lambda^t, \text{ and } \mathcal{C}_i^t, i = 0, 1, \dots, 7\}.$$

And the forwarding process of QISTA-Net-n (QISTA-Net for reconstructing the Natural image) is shown in Algorithm 3.

In the forwarding process of QISTA-Net-n, step 2 is similar to as step 2 plus step 3 in QISTA-Net-s (Algorithm 2). The difference is that, in QISTA-Net-s, the βA^T is setting to be the training variables \mathcal{A}^t (independent among each layer) and keep A fixed as a constant matrix, whereas in QISTA-Net-n, all of the β , A^T , and A are setting to be the training variables β^t , \mathcal{B} , and \mathcal{A} , respectively. Note that \mathcal{A} and \mathcal{B} in QISTA-Net-n are common used in each layer, and β^t is independent among each layer.

Algorithm 3 QISTA-Net-n

- 1: **for** $t = 1$ to T **do**
 - 2: $r^t = x^{t-1} + \beta^t \mathcal{B} (y - \mathcal{A}x^{t-1});$
 - 3: $\gamma_i^t = \frac{\lambda^t}{(|\Psi^t(\mathcal{C}_0^t(r^t))_i| + \varepsilon_i)^{1-q}}, \forall i \in [1 : n];$
 - 4: $x^t = r^t + \alpha^t \mathcal{C}_7^t \left(\tilde{\Psi}^t (\eta(\Psi^t(\mathcal{C}_0^t(r^t)); \gamma^t) - \Psi^t(\mathcal{C}_0^t(r^t))) \right);$
 - 5: **end for**
-

4.4. Loss Function

In general, the loss function of the learning-based method is to consider MSE-loss as in Eq. (17). However, in Sec. 4.1, we relaxed the Ψ^T as $\bar{\gamma}\Psi^\dagger$, therefore we restrict the left-inverse relation between Ψ and $\tilde{\Psi}$ in each layer $t = 1, 2, \dots, T$ as

$$\mathcal{L}_{\text{aux}} = \sum_{t=1}^T \left\| \tilde{\Psi}^t \circ \Psi^t - I \right\|_2^2,$$

which is implemented by

$$\mathcal{L}_{\text{aux}} = \sum_{t=1}^T \left\| \tilde{\Psi}^t (\Psi^t(w^t)) - w^t \right\|_2^2,$$

where $w^t = \mathcal{C}_0^t(r^t)$ in the t^{th} -layer. Together with \mathcal{L}_{MSE} , the loss function of QISTA-Net-n is designed as follows:

$$\mathcal{L} = \mathcal{L}_{\text{MSE}} + \delta \mathcal{L}_{\text{aux}},$$

where $\delta > 0$ is a constant.

5. EXPERIMENTAL RESULTS OF ITERATIVE METHOD FOR SOLVING THE SPARSE SIGNAL RECONSTRUCTION PROBLEM

In this section, we show the reconstruction performance of QISTA in Algorithm 1 that solving the sparse signal reconstruction problem in the conventional iterative optimization style and compare the performance with state-of-the-art iterative sparse signal reconstruction methods.¹

5.1. Parameter Setting

For fair comparison, we followed the same setting as in [15] that the problem dimensions were $n = 1024$ and $m = 256$, and the ground-truth $x_0 \in \mathbb{R}^n$ was k -sparse signal, where the non-zero entries followed i.i.d. Gaussian distribution $\mathcal{N}(0, 1)$. For the sensing matrix $A \in \mathbb{R}^{m \times n}$, its entries $A_{i,j}$'s followed i.i.d. Gaussian distribution $\mathcal{N}(0, 1)$ (without column normalization).

The parameters in QISTA were $\beta = \frac{1}{\|A\|_2^2}$, where $\|A\|_2$ is the spectral norm of A , $\lambda = 10^{-4} \cdot \beta$, $q = 0.05$, and $\varepsilon = \mathbf{1}_n$, where $\mathbf{1}_n$ is a vector in \mathbb{R}^n with each component being equal to 1.

¹All of our implementation codes (including of in Sec. 6 and 7) can be downloaded from <https://github.com/spybeiman/QISTA-Net/>

5.2. Performance Comparison of Reconstructing The Synthesize Data

We compare the proposed method, QISTA, with traditional iterative methods IHT [10], FISTA [13] (ISTA [5] was not included because both ISTA and FISTA have exactly the same reconstruction performance), half thresholding algorithm [12], 2/3 algorithm [16], and $1/2 - \epsilon$ algorithm [15]. The criterion, declaring a successful perfect reconstruction of the ground-truth if the relative error $RE = \frac{\|x^* - x_0\|_2}{\|x_0\|_2} \leq 10^{-4}$ holds [15], was adopted. In Fig. 2, the results were shown in terms of the success rate averaged at 20 tests vs. sparsity k . We can see that QISTA can perfect reconstruct the ground-truth until k is 94 (in this case, $3k = 282 > m$) but LASSO fails to recover the ground-truth [6]. The $1/2 - \epsilon$ algorithm [15] perfectly reconstructs the ground-truth until k is around 68. The reconstruction performance of QISTA outperforms these state-of-the-art ℓ_q -based algorithms in terms of success rate. Remark that AMP [14] was not included for comparison because, under the setting of sensing matrix A without column normalization, it does not converge.

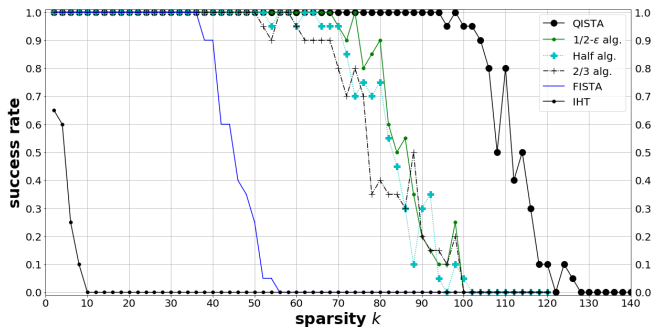


Fig. 2: The success rates of QISTA, $1/2 - \epsilon$ algorithm, half thresholding algorithm, 2/3 algorithm, FISTA, and IHT in reconstructing the exactly k -sparse ground-truth with $n = 1024$, $m = 256$, and various k .

6. EXPERIMENTAL RESULTS OF DEEP LEARNING-BASED METHOD FOR SOLVING THE SPARSE SIGNAL RECONSTRUCTION PROBLEM

In this section, we show the reconstruction performance of QISTA-Net-s in Algorithm 2 that solving the sparse signal reconstruction problem in the deep learning-based style and compare the performance with state-of-the-art deep learning-based sparse reconstruction methods. The QISTA-Net-s were conducted on the device NVIDIA Geforce GTX 1060 GPU, on the platform Python 3.6 with Pytorch version 0.4.1.

6.1. Parameter Setting

For fair comparison, we followed the same setting as in [18, 19, 33] that the problem dimensions were $n = 500$, $m = 250$. The entries of the ground-truth $x_0 \in \mathbb{R}^n$ (which is a k -sparse signal) followed i.i.d. Gaussian distribution $\mathcal{N}(0, 1)$ with probability 10% (that is x_0 is Bernoulli-Gaussian with $k \approx n \times 10\% = 50$). For the sensing matrix $A \in \mathbb{R}^{m \times n}$, its entries $A_{i,j}$'s followed i.i.d. Gaussian distribution with column normalization $\mathcal{N}(0, \frac{1}{m})$.

The constant parameters in QISTA-Net-s were $\beta = \frac{1}{\|A\|_2^2}$, $q = 0.05$, and $\gamma = 0.1$. The training parameters of QISTA-Net-s were initialized as $\lambda^t = 10^{-4} \cdot \beta$, $A^t = \beta A^T$, and $\mathcal{E}^t = 0.1 \cdot \mathbf{1}_n$ for each layer t . In addition, since \mathcal{E}_i^t plays the same role with ε_i in Eq. (5), and the value of \mathcal{E}_i^t may be negative after doing back-propagation, we further restrict \mathcal{E}_i^t after each back-propagation to remain positive by letting $\mathcal{E}_i^t = \max\{\mathcal{E}_i^t, 0.1\}$.

6.2. Performance Comparison of Reconstructing The Synthesize Data

In this section, we conducted comparisons of QISTA-Net-s with state-of-the-art deep learning-based sparse signal reconstruction methods, including LAMP tied [18] and LAMP untied [18], LISTA-CP [19], LISTA-SS [19], and LISTA-CPSS [19], ALISTA [33] and TiLISTA [33], and TISTA [20], in Fig. 3, Fig. 4, Fig. 5, and Fig. 6. Remark that we only compare with the ℓ_1 -based methods because, to our knowledge, we have not found any ℓ_q -based ($0 < q < 1$) learning-based methods. The results of LAMP-tied, LAMP-untied, LISTA-CP, LISTA-SS, LISTA-CPSS, TiLISTA, ALISTA, and TISTA were obtained by applying the codes provided by the corresponding authors. Moreover, LISTA (which is the comparison target in [18, 19, 33, 20]) was not selected because all of the network models, we adopted to compare with, have already completely outperformed it (including LISTA [17] that shares the learning parameters S and B for each layer, and LISTA [18] that learns A^t and B^t in each layer independently) in terms of reconstruction quality. The reconstruction quality was measured by Signal-to-Noise-Ratio (SNR = $10 \log_{10} \left(\frac{\|x_0\|_2^2}{\|x^* - x_0\|_2^2} \right)$ dB). All of the reconstruction results of QISTA-Net-s are of the averaged at 100 tests.

In Fig. 3, we show the performance comparison between QISTA-Net-s and the other state-of-the-art ℓ_1 -based DNN methods, in reconstructing the exactly k -sparse ground-truth ($n = 500$, $m = 250$, and $k \approx 50$). We can see that QISTA in Sec. 2 is the iterative method whereas QISTA-Net-s is its accelerated version via DNN architecture. At the 16th iteration (layer), the reconstruction performance of QISTA-Net-s is still good. The performance comparison of reconstructing the exactly k -sparse ground-truth under measurement rate 30% ($n = 500$, $m = 150$, and $k \approx 50$) is shown in Fig. 4. In Fig. 5, we demonstrate the performance comparison

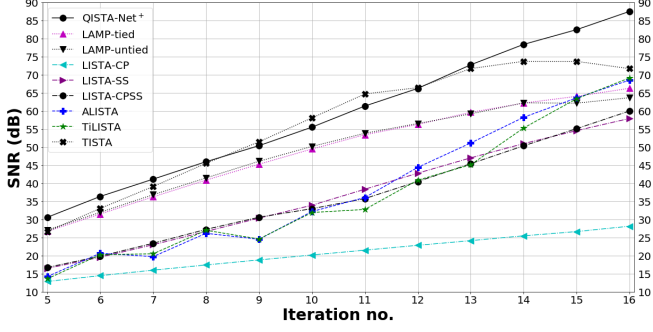


Fig. 3: Comparison in reconstructing the exactly k -sparse ground-truth, with measurement rate 50% ($n = 500, m = 250$).

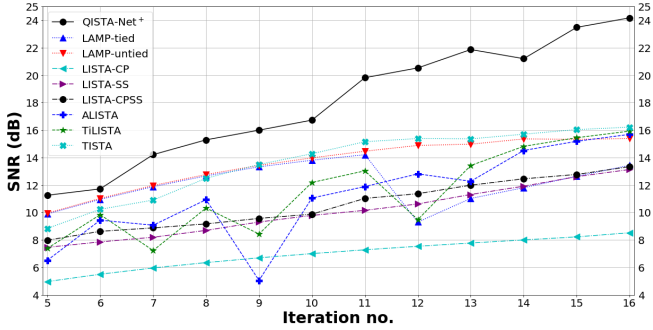


Fig. 4: Comparison in reconstructing the exactly k -sparse ground-truth, with measurement rate 30% ($n = 500, m = 150$).

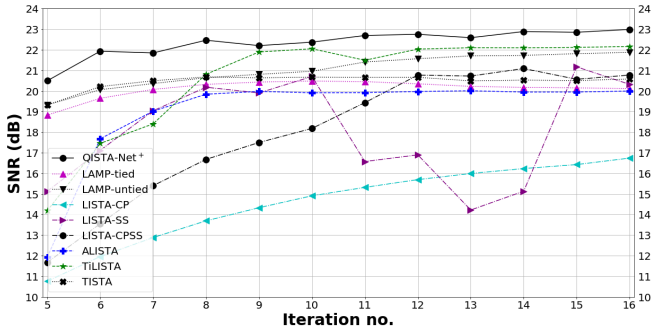


Fig. 5: Comparison in reconstructing the ground-truth at measurement noise SNR=20dB with measurement rate 50% ($n = 500, m = 250$).

in reconstructing the ground-truth with measurement noise at SNR=20dB ($n = 500, m = 250$, and $k \approx 50$). In general, the ℓ_q -norm (and also ℓ_0 -norm) minimization problem is considered not robust, that is, if the original signal is noisy, the reconstruction result is considered to be unreliable (in

comparison with the result of ℓ_1 -norm). But, as shown in Fig. 5, QISTA-Net-s still outperforms all the ℓ_1 -norm learning-based methods, this is because the network architecture of QISTA-Net-s is also including the method to solve the ℓ_1 -norm problem. Finally, in Fig. 6, we show the comparison results in terms of running time (sec.) vs. reconstruction performance (SNR (dB)) at measurement noise SNR=20dB under $n = 500, m = 250$, and $k \approx 50$.

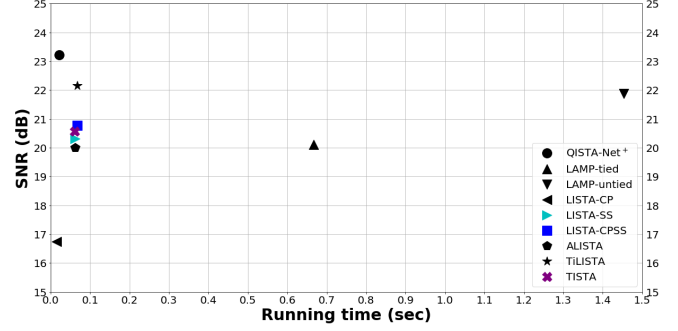


Fig. 6: Running time vs. Reconstruction performance at measurement noise SNR=20dB with measurement rate 50% ($n = 500, m = 250$) at 16th iteration/layer of Fig. 5.

In summary, we can see from Fig. 3, Fig. 4, and Fig. 5 that QISTA-Net-s outperforms all the other existing works in terms of reconstruction quality. Moreover, in Fig. 4, all the ℓ_1 -based DNN methods used for comparison only achieve a maximum of 17dB (at 16th layer). We conjecture that this is because, for the ℓ_1 -based iterative methods, m must be greater than $3k$ to achieve a good reconstruction performance [6]. Furthermore, Fig. 6 actually indicates that QISTA-Net-s offers state-of-the-art performance in terms of reconstruction quality and speed.

6.3. Ablation Study

In the sparse signal reconstruction problem, the (ℓ_0) -problem (in Eq. (2)) is commonly used to find the sparse ground-truth. Due to the NP-hard property of the (ℓ_0) -problem, it is always adopting LASSO (in Eq. (3)) to approximate the (ℓ_0) -problem in the literature. In this paper, we challenge the (ℓ_q) -problem (in Eq. (4)), $0 < q < 1$, which is non-convex, to approximate the (ℓ_0) -problem.

In Sec. 3, we designed a learning-based method, QISTA-Net-s, to solve the (ℓ_q) -problem. In Fig. 7, we demonstrate the reconstruction performance of QISTA-Net-s with respect to q . The dimension setting is $n = 500$ and $m = 250$ (the measurement rate is 50%). The other parameter setting is followed in Sec. 6.1. We observe that reconstruction quality is increased when q is decreased. This indicates that in solving the (ℓ_q) -problem is better approaches the ℓ_0 -norm minimization problems than its ℓ_1 -norm counterpart, as suggested in [6, 7].

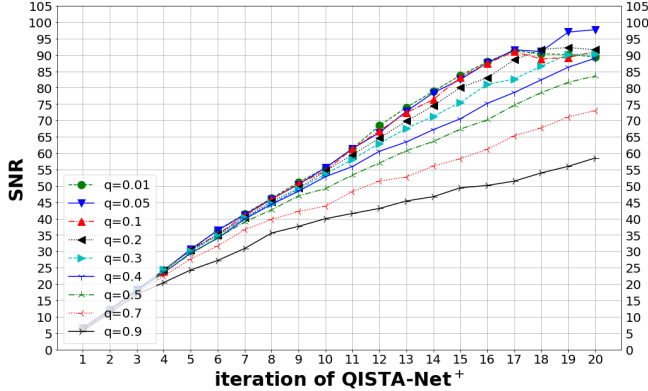


Fig. 7: QISTA-Net-s in reconstructing the exactly k -sparse ground-truth, with measurement rate 50% ($n = 500, m = 250$), under various q 's.

In Sec. 2, we proposed an iterative algorithm QISTA in solving the sparse signal reconstruction problem. In Sec. 3, we designed a DNN method by unfolding the parameters in QISTA, as shown in Eq. (16), to accelerate the reconstruction process. After unfolding QISTA, we further accelerated by considering the momentum coming from the descent direction of all previous layers, and the result was QISTA-Net-s (in Algorithm 2).

In Fig. 8, we study the effect of the momentum coming from all of the previous layers. That is, we compare the network architecture in Algorithm 2 with the network architecture in Eq. (16) (we call QISTA-unfold for convenient). The dimension setting is $n = 500$. We compare the two tasks in two measurement rates, 50% ($m = 250$), and 30% ($m = 150$). The other parameter setting is followed in Sec. 6.1. All of the results are presented in an average of 100 tests.

As shown in Fig. 8, we can see that, under the same SNR values, QISTA-Net-s needs fewer layers than QISTA-unfold. As $m = 250$, to reach SNR=80dB, QISTA-Net-s took only 16 layers but QISTA-unfold needs 19 layers, and then the two have a similar reconstruction performance after 23rd layer. Moreover, when $m = 150$, the improvement of QISTA-Net-s is significant. This indicates that the speed-up strategy of momentum is effective.

7. EXPERIMENTAL RESULTS OF DEEP LEARNING-BASED METHOD IN RECONSTRUCTING THE NATURAL IMAGES

In this section, we show the reconstruction performance of QISTA-Net-n in Algorithm 3 that reconstructing the natural images in the deep learning-based method and compare the performance with state-of-the-art deep learning-based methods.

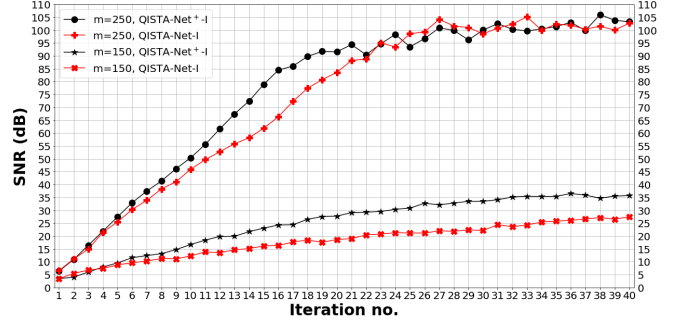


Fig. 8: Performance comparison between QISTA-Net-s and QISTA-unfold in reconstructing the exactly k -sparse ground-truth under measurement rates 50% and 30%.

Table 1: The list of input feature and output feature.

	C_0	C_1	C_2	C_3	C_4	C_5	C_6	C_7
Input feature	1	32	32	32	32	32	32	32
Output feature	32	32	32	32	32	32	32	1

7.1. Parameter Setting

The constant parameter in QISTA-Net-n was $\varepsilon = 0.1 \cdot \mathbf{1}_n$. The training parameters of QISTA-Net-n were initialized as $\beta^t = 0.1$, $\lambda^t = 10^{-5}$, $\alpha^t = 1$, and the others $\{\mathcal{B}, \mathcal{A}, \text{ and } \mathcal{C}_i^t, i = 0, 2, \dots, 7\}$ were initialized by xavier initializer [34].

For the convolutional dictionaries Ψ and $\tilde{\Psi}$, together with the extras C_0 and C_7 , all the kernels of convolution operators were set to 3×3 , and the numbers of input features and output features of $C_0, C_1, C_2, C_3, C_4, C_5, C_6$, and C_7 are listed in Table 1.

7.2. Datasets for Training and Testing

In the experiment to reconstruct the natural image, the training dataset is the Set91 (91 images) database; the Set11 (11 images) database is adopted for validation data; and the Set5 (5 images), Set14 (14 images), BSD68 (68 images), and BSD100 (100 images) databases are the testing datasets.

The training data is generated by cropping the 64×64 pixels sub-images with the stride of 7, of each image in Set91, into 68,323 sub-images. Moreover, the training data is augmented by flipped, rotation 90, rotation 90 plus flipped, rotation 180, rotation 180 plus flipped, rotation 270, and rotation 270 plus flipped, to each sub-image, with finally 546,584 sub-images.

7.3. Training Details

For a fair comparison, we adopt a similar training setting with SCSNet [27] (and also with CSNet⁺ [26] because both of

them has the same training setting) that the measurement matrix A operating on the image block with block size 32×32 . This will require us to do the necessary pre-processing and post-processing in step 2 of QISTA-Net-n. We follow the training setting in SCSNet because it had the best reconstruction performance in the comparison object. The training batch in the proceeding is in image-shape, in size of $64 \times 64 \times b$, where b is the training batch size, and 64×64 is the size of a training data. The required processing is as follows. To simplify the illustration, here we suppose the batch size $b = 1$.

1. In step 2 of QISTA-Net-n, since the operator \mathcal{A} is unfolding by $A \in \mathbb{R}^{m \times 1024}$, and the input x^{t-1} of step 2 has the size of 64×64 , we first divide the sub-image x^{t-1} into 4 blocks, each of such has the size of 32×32 . Next, we reshape each of the blocks into vector-form \mathbb{R}^{1024} (4 vectors: x_1, x_2, x_3, x_4), then multiple each of x_i by $\mathcal{A} \in \mathbb{R}^{m \times 1024}$ (the measurement rate $\frac{m}{1024}$), and get the results $y_i = \mathcal{A}x_i \in \mathbb{R}^m, i = 1, 2, 3, 4$. The size of the object in the process is as shown in the following.

$$64 \times 64 \xrightarrow{\text{divide}} 32 \times 32 \times 4 \rightarrow 1024 \times 4 \xrightarrow{\mathcal{A}} m \times 4 \quad (31)$$

2. For operator \mathcal{B} in step 2, we see that the size of $y - \mathcal{A}x^{t-1}$ is $m \times 4$. Since \mathcal{B} is unfolding by $A^T \in \mathbb{R}^{1024 \times m}$, we have $\mathcal{B}(y - \mathcal{A}x^{t-1}) \in \mathbb{R}^{1024 \times 4}$. After the operating of \mathcal{B} , we reverse the pre-processing that we did before \mathcal{A} , which leads the results back into the image-form of the size 64×64 . The size of the object in the process we do is as shown in the following.

$$m \times 4 \xrightarrow{\mathcal{B}} 1024 \times 4 \rightarrow 32 \times 32 \times 4 \xrightarrow{\text{merge}} 64 \times 64 \quad (32)$$

The pre-process as in Eq. (31), and the post-process as in Eq. (32) is to reduce the memory cost of measurement matrix \mathcal{A} (we will adopt \mathcal{A} as the measurement matrix after the training finished). When we sense an image, assuming that the measurement rate is r_0 , no matter whether the image block size is 64×64 or 32×32 , the sampling rate is the same, but the required storage cost for measurement matrix \mathcal{A} is different. If the image block size is 64×64 , \mathcal{A} has the size of $m \times 4096$, whereas if the image block size is 32×32 , \mathcal{A} has the size of $m \times 1024$.

The training data consists of 273,292 sub-images in size of 64×64 pixels. In each batch, we randomly choose 64 sub-images from the training data to train. Remark that the image block size we adopt in this paper is 64×64 instead of 96×96 as in SCSNet [27] due to the restriction of device memory.

7.4. Performance Comparison of Reconstructing The Natural Image

The experiments in this subsection were conducted on Intel Core i7-7700 CPU plus a NVIDIA GeForce GTX 1080 Ti GPU, Python with TensorFlow version 1.14.0.

In this subsection, we compare the reconstruction performance with state-of-the-art learning-based methods including SDA [21], ReconNet [22], ISTA-Net+ [28], MS-CSNet [23], DR²-Net [24], $\{0, 1\}$ -BCSNet [26], $\{-1, +1\}$ -BCSNet [26], CSNet+ [26], SCSNet [27], MSRNet [25], method in [35], method in [36], and method in [29]. The comparison results are shown in Table 2, Table 3, Table 4, Table 5, and Table 6, which are corresponding to the datasets Set11, BSD68, Set5, Set14, and BSD100, respectively. In each dataset, the best reconstruction results are marked in bold font. The reconstruction results of the comparison objects (in PSNR and SSIM) are obtained by the experiment results of the corresponding papers. The “dash” mark in the tables means the authors did not provide.

Table 2 shows the comparison of reconstruction performance in terms of PSNR of different learning-based methods on various measurement rates. Because Set11 is adopted as the validation data, QISTA-Net-n obtains better reconstruction performance in terms of PSNR than the comparison objects therein.

In Table 3, we compare the reconstruction performance in terms of PSNR with other learning-based methods. In Table 4, Table 5, and Table 6, we compare the reconstruction performance in both PSNR and SSIM with other learning-based methods. The reconstruction performance of QISTA-Net-n in terms of PSNR outperforms the other methods in all measurement rates therein, except the 1% measurement rate. For 1% measurement rate, SCSNet has the best reconstruction performance in PSNR. We guess this is because SCSNet adopts the sub-images in size of 96×96 pixels as the input of the network architecture, and this implies that SCSNet has less blocking artifact effect. However, QISTA-Net-n cannot take the sub-images in the size of 96×96 pixels as the training data due to limitations on the memory size of the GPUs. On the other hand, the reconstruction performance of QISTA-Net-n in terms of SSIM, although not better than all of the other methods, but it has almost the same as the best one.

Fig. 11, Fig. 9, and Fig. 10 show the visual comparison between ground-truth and the reconstruction results of CSNet+, SCSNet, and QISTA-Net-n. We do not compare with the other methods because either the authors do not provide the implementation codes or the visual comparison in [27] is already done with obviously comparison results. Besides, we compare with only CSNet+ and SCSNet because the comparison results of these two methods almost overwhelming the other related works. “Monarch” in Fig. 9 is from the dataset Set11, whereas “ppt3” in Fig. 10 and “barbara” in Fig. 11 are from the dataset Set14. Fig. 9 show the comparison results between CSNet+, SCSNet, and QISTA-Net-n, in reconstruct the “Monarch” image from the dataset Set14, with measurement rate 10%. We can see that the reconstruction result of QISTA-Net-n at the Butterfly’s tentacles is relatively not blurred. Fig. 10 show the results in reconstruct the “ppt3” image from the dataset Set14, with mea-

surement rate 10%. We can clearly recognize the letter E at the reconstruction result of QISTA-Net-n. Fig. 11 show the results in reconstruct the “barbara” image from the dataset Set14, with measurement rate 20%. In the reconstruction result of QISTA-Net-n, the texture of the tablecloth is closer to the original pattern. On the contrary, the other two methods are a bit sharp in the upper right-lower left texture. Moreover, in the comparison between Fig. 11 (g)-(i), we can see that QISTA-Net-n tries to reconstruct the striped texture.

7.5. Running Time Comparison of Reconstructing The Natural Images

Table 7 show the average running time in reconstructing a 256×256 image. The running time of the comparison objects are taken from [26] and [27]. We can see that the running time of QISTA-Net-n in GPU is close to CSNet⁺, but the performance is better than CSNet⁺ in most cases. Besides, in comparison with SCSNet, Qista-Net-n also obtains better performance in most cases, but the running time of Qista-Net-n is 5 times faster than CS.

8. CONCLUSION AND FUTURE WORK

In this paper, we first reformulate the ℓ_q -norm minimization problem into a 2-step problem (7), which excludes the difficulties coming from the non-convexity.

We then propose QISTA to solve the (ℓ_q) -problem via the ℓ_1 -norm based iterative algorithm. The QISTA obtains reasonable result associated with suggestion of (ℓ_q) -problem in that the smaller q leads to the better reconstruction performance. Moreover, with the help of deep learning strategy and “momentum” strategy, we propose an ℓ_q learning-based method, QISTA-Net-s. The resultant QISTA-Net-s retains better reconstruction performance and faster reconstruction speed than state-of-the-art ℓ_1 -norm DNN methods, even if the original sparse signal is noisy. Finally, with the help of convolution neural network, we proposed the QISTA-Net-n to solve the image CS problem. The reconstruction performance outperforms most of the state-of-the-art natural images reconstruction methods.

9. REFERENCES

- [1] E. J. Candès, J. Romberg, and T. Tao, “Robust uncertainty principles: exact signal reconstruction from highly incomplete frequency information,” *IEEE Trans. Inf. Theory*, vol. 52, no. 2, pp. 489–509, 2006.
- [2] D. L. Donoho, “Compressed sensing,” *IEEE Trans. Inf. Theory*, vol. 52, no. 4, pp. 1289–1306, 2006.
- [3] B. K. Natarajan, “Sparse approximate solutions to linear systems,” *SIAM J. Comput.*, vol. 24, no. 2, pp. 227–234, 1995.
- [4] J. L. Starck, D. L. Donoho, and E. J. Candès, “Astronomical image representation by the curvelet transform,” *Astron. Astrophys.*, vol. 398, no. 2, pp. 785–800, 2003.
- [5] I. Daubechies, M. Defrise, and C. De Mol, “An iterative thresholding algorithm for linear inverse problems with a sparsity constraint,” *Commun. Pure Appl. Math.*, vol. 57, no. 11, pp. 1413–1457, 2004.
- [6] R. Chartrand, “Exact reconstruction of sparse signals via nonconvex minimization,” *IEEE Signal Process. Lett.*, vol. 14, no. 10, pp. 707–710, 2007.
- [7] R. Chartrand and W. Yin, “Iteratively reweighted algorithms for compressive sensing,” *In Proc. Int. Conf. Acoustics, Speech, Signal Processing (ICASSP)*, 2008.
- [8] D. Ge, X. Jiang, and Y. Ye, “A note on the complexity of ℓ_p minimization,” *Math. Program. Series B*, vol. 129, no. 2, pp. 285–299, 2011.
- [9] L. Zheng, A. Maleki, H. Weng, X. Wang, and T. Long, “Does ℓ_p -minimization outperform ℓ_1 -minimization?,” *IEEE Trans. Inf. Theory*, vol. 63, no. 11, pp. 6896–6935, Nov. 2017.
- [10] T. Blumensath and M. E. Davies, “Iterative thresholding for sparse approximations,” *J. Fourier Anal. Appl.*, vol. 14, no. 5–6, pp. 629–654, 2008.
- [11] F. Wen, L. Chu, P. Liu, and R. C. Qiu, “A survey on non-convex regularization-based sparse and low-rank recovery in signal processing, statistics, and machine learning,” *IEEE Access*, vol. 6, pp. 69883–69906, Nov. 2018.
- [12] Z. Xu, X. Chang, F. Xu, and H. Zhang, “ $\ell_{1/2}$ regularization: A thresholding representation theory and a fast solver,” *IEEE Trans. Neural Netw. Learn. Syst.*, vol. 23, no. 7, pp. 1013–1027, 2012.
- [13] A. Beck and M. Teboulle, “A fast iterative shrinkage-thresholding algorithm for linear inverse problems,” *SIAM J. Imaging Sci.*, vol. 2, no. 1, pp. 183–202, 2009.
- [14] D. L. Donoho, A. Maleki, and A. Montanari, “Message-passing algorithms for compressed sensing,” *Proc. Natl. Acad. Sci. U.S.A.*, vol. 106, no. 45, pp. 18914–18919, 2009.
- [15] A. Cui, J. Peng, H. Li, M. Wen, and J. Jia, “Iterative thresholding algorithm based on non-convex method for modified ℓ_p -norm regularization minimization,” *J. Comput. Appl. Math.*, vol. 347, pp. 173–180, Feb. 2019.
- [16] W. Cao, J. Sun, and Z. Xu, “Fast image deconvolution using closed-form thresholding formulas of $\ell_q(q = \frac{1}{2}, \frac{2}{3})$ regularization,” *J. Vis. Commun. Image Represent.*, vol. 24, no. 1, pp. 31–41, 2013.

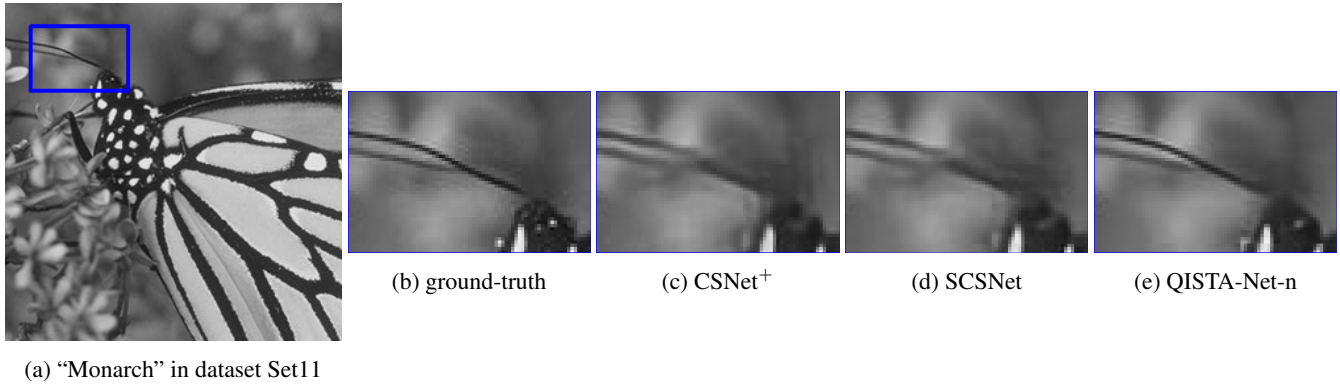


Fig. 9: Reconstruction Result of CSNet⁺, SCSNet, and QISTA-Net-n with 10% measurement rate.

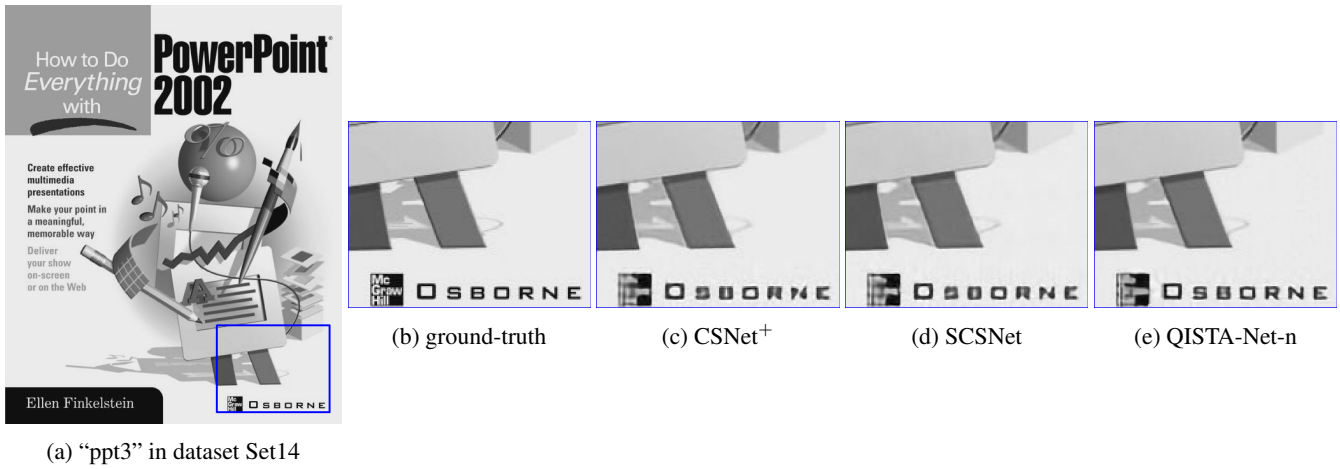


Fig. 10: Reconstruction Result of CSNet⁺, SCSNet, and QISTA-Net-n with 10% measurement rate.

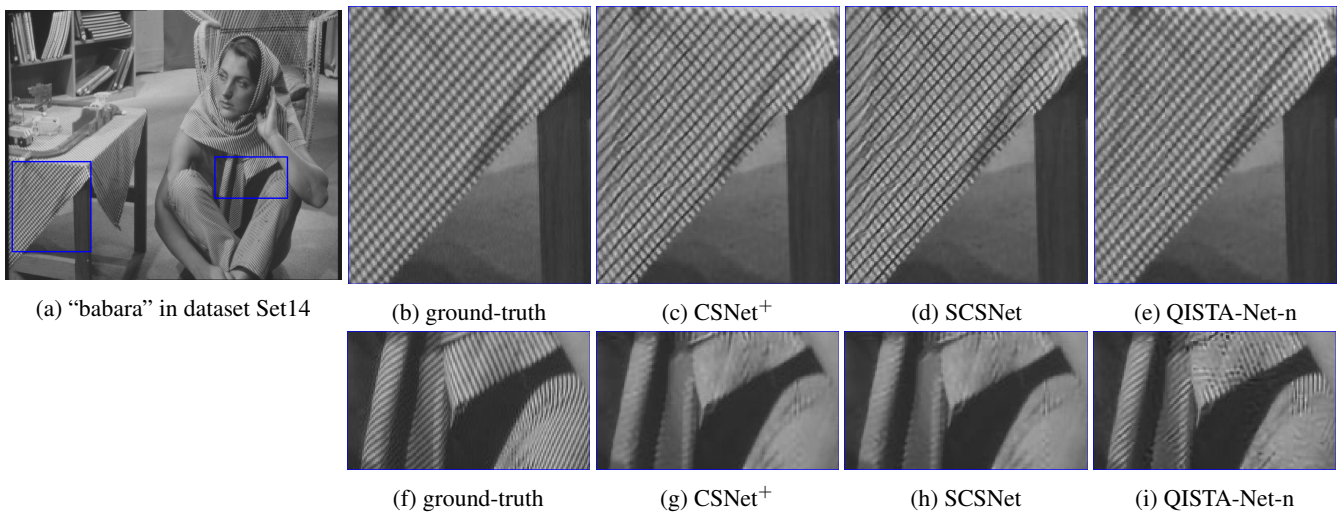


Fig. 11: Reconstruction Result of CSNet⁺, SCSNet, and QISTA-Net-n with 20% measurement rate.

Table 2: Average PSNR (dB) comparisons of different methods with various measurement rates on Set11.

measurement rate	50%	40%	30%	25%	10%	4%	1%
SDA [21]	28.95	27.79	26.63	25.34	22.65	20.12	17.29
ReconNet [22]	31.50	30.58	28.74	25.60	24.28	20.63	17.27
[36]	36.23	34.06	31.18	30.07	24.02	17.56	7.70
LISTA-CPSS [19]	34.60	32.87	30.54	-	-	-	-
ISTA-Net ⁺ [28]	38.07	36.06	33.82	32.57	26.64	21.31	17.34
DR ² -Net [24]	-	-	-	29.06	24.71	21.29	17.80
{0, 1}-BCSNet [26]	35.05	34.61	32.57	-	26.39	-	20.62
{-1, +1}-BCSNet [26]	35.57	34.94	33.42	-	28.03	-	20.93
CSNet ⁺ [26]	38.52	36.48	34.30	-	28.37	-	21.03
SCSNet [27]	39.01	36.92	34.62	-	28.48	-	21.04
MSRNet [25]	-	-	-	33.36	28.07	24.23	20.08
[29]	-	-	-	32.81	26.97	-	18.83
QISTA-Net-n	40.30	38.32	36.09	34.84	29.79	25.95	21.29

Table 3: Average PSNR (dB) comparisons of different methods with various measurement rates on BSD68.

measurement rate	50%	40%	30%	25%	10%	4%	1%
SDA [21]	28.35	27.41	26.38	-	23.12	21.32	-
ReconNet [22]	29.86	29.08	27.53	-	24.15	21.66	-
ISTA-Net ⁺ [28]	34.01	32.21	30.34	-	25.33	22.17	-
CSNet [26]	34.89	32.53	31.45	-	27.1	-	22.34
SCSNet [27]	35.77	33.86	31.87	-	27.28	-	22.37
[29]	-	-	-	29.54	-	-	-
QISTA-Net-n	36.56	34.58	32.64	31.63	27.83	25.24	22.23

Table 4: Average PSNR (dB) and SSIM comparisons of different methods with various measurement rates on Set5.

Set5 dataset	PSNR SSIM	PSNR SSIM	PSNR SSIM	PSNR SSIM	PSNR SSIM	PSNR SSIM	PSNR SSIM
measurement rate	50%	40%	30%	20%	10%	5%	1%
ReconNet [22]	- -	- -	- -	- -	25.98 0.734	- -	- -
[35]	- -	- -	36.54 0.956	34.55 0.939	31.31 0.894	- -	- -
MS-CSNet [23]	- -	- -	38.43 0.966	36.26 0.950	32.82 0.909	- -	- -
DR ² -Net [24]	- -	- -	- -	- -	27.79 0.798	- -	- -
{0, 1}-BCSNet [26]	38.69 0.970	38.24 0.967	36.44 0.955	32.31 0.898	29.99 0.851	28.57 0.816	23.79 0.636
{-1, +1}-BCSNet [26]	39.23 0.967	38.62 0.964	37.22 0.956	35.24 0.939	32.20 0.898	29.39 0.840	24.07 0.645
CSNet ⁺ [26]	41.79 0.980	40.11 0.974	38.25 0.964	36.05 0.948	32.59 0.906	29.74 0.849	24.18 0.648
SCSNet [27]	42.22 0.982	40.44 0.976	38.45 0.966	36.15 0.949	32.77 0.908	29.74 0.847	24.21 0.647
QISTA-Net-n	43.17 0.982	41.27 0.975	39.24 0.966	37.04 0.951	33.63 0.917	30.23 0.863	23.60 0.650

Table 5: Average PSNR (dB) and SSIM comparisons of different methods with various measurement rates on Set14.

Set14 dataset	PSNR SSIM	PSNR SSIM	PSNR SSIM	PSNR SSIM	PSNR SSIM	PSNR SSIM	PSNR SSIM
measurement rate	50%	40%	30%	20%	10%	5%	1%
ReconNet [22]	- -	- -	- -	- -	24.18 0.640	- -	- -
[35]	- -	- -	33.08 0.926	31.21 0.885	28.54 0.814	- -	- -
MS-CSNet [23]	- -	- -	34.34 0.930	32.26 0.896	29.29 0.820	- -	- -
DR ² -Net [24]	- -	- -	- -	- -	24.38 0.706	- -	- -
{0, 1}-BCSNet [26]	35.01 0.945	34.52 0.938	32.68 0.912	29.25 0.816	27.36 0.756	26.09 0.694	22.48 0.553
{-1, +1}-BCSNet [26]	35.56 0.944	34.81 0.934	33.47 0.916	31.55 0.880	28.78 0.805	26.67 0.724	22.74 0.562
CSNet ⁺ [26]	37.89 0.963	36.16 0.950	34.34 0.930	32.15 0.894	29.13 0.817	26.93 0.733	22.83 0.563
SCSNet [27]	38.41 0.966	36.54 0.953	34.51 0.931	32.19 0.895	29.22 0.818	26.92 0.732	22.87 0.563
QISTA-Net-n	39.61 0.969	37.57 0.955	35.49 0.936	33.18 0.903	29.97 0.829	27.51 0.747	22.63 0.564

Table 6: Average PSNR (dB) and SSIM comparisons of different methods with various measurement rates on BSD100.

BSD100 dataset	PSNR SSIM	PSNR SSIM	PSNR SSIM	PSNR SSIM	PSNR SSIM	PSNR SSIM	PSNR SSIM	PSNR SSIM
measurement rate	50%	40%	30%	20%	10%	5%	1%	
MS-CSNet [23]	- -	- -	33.19 0.919	31.15 0.874	28.61 0.786	- -	- -	- -
{0, 1}-BCSNet [26]	33.95 0.937	33.41 0.928	31.67 0.894	28.65 0.785	27.05 0.722	26.04 0.658	23.49 0.541	
{-1, +1}-BCSNet [26]	34.57 0.940	33.67 0.925	32.28 0.899	30.50 0.855	28.21 0.770	26.55 0.689	23.70 0.547	
CSNet+ [26]	36.68 0.962	34.91 0.944	33.08 0.917	31.05 0.872	28.53 0.783	26.78 0.698	23.76 0.548	
SCSNet [27]	37.14 0.965	35.21 0.947	33.24 0.919	31.10 0.873	28.57 0.784	26.77 0.697	23.78 0.548	
QISTA-Net-n	37.55 0.964	35.60 0.946	33.66 0.919	31.53 0.875	28.87 0.788	26.95 0.703	23.46 0.543	

Table 7: Average running time (in seconds) of different methods for reconstructing a 256×256 image.

measurement rate	1%		10%		Programming Language
	CPU	GPU	CPU	GPU	
SDA [21]	-	0.0045	-	0.0029	Matlab + caffe
ReconNet [22]	0.5193	0.0244	0.5258	0.0195	
ISTA-Net+ [28]	1.3750	0.0470	1.3750	0.0470	Python + TensorFlow
{0, 1}-BCSNet [26]	0.9066	0.0275	0.9081	0.0281	Matlab + Matconvnet
{-1, +1}-BCSNet [26]	0.9115	0.0274	0.9065	0.0276	
CSNet+ [26]	0.8960	0.0262	0.9024	0.0257	
SCSNet [27]	0.5103	0.1050	0.5146	0.1332	Matlab + Matconvnet
QISTA-Net-n	0.7620	0.0255	0.7575	0.0238	Python + TensorFlow

- [17] K. Gregor and Y. LeCun, "Learning fast approximations of sparse coding," *In Proc. Int. Conf. Machine Learning (ICML)*, 2010.
- [18] M. Borgerding, P. Schniter, and S. Rangan, "Amp-inspired deep networks for sparse linear inverse problems," *IEEE Trans. Signal Process.*, vol. 65, no. 16, pp. 4293–4308, Aug. 2017.
- [19] X. Chen, J. Liu, Z. Wang, and W. Yin, "Theoretical linear convergence of unfolded ISTA and its practical weights and thresholds," *In Adv. Neural. Inf. Process. Syst. (NeurIPS)*, Dec. 2018.
- [20] D. Ito, S. Takabe, and T. Wadayama, "Trainable ISTA for sparse signal recovery," *IEEE Trans. Signal Process.*, vol. 67, no. 12, pp. 3113–3125, 2019.
- [21] A. Mousavi, A. B. Patel, and R. G. Baraniuk, "A deep learning approach to structured signal recovery," *In Proc. Annu. Allerton Conf. Commun., Control, and Comput. (Allerton)*, Sep. 2015.
- [22] K. Kulkarni, S. Lohit, P. Turaga, R. Kerviche, and A. Ashok, "Reconnet: Non-iterative reconstruction of images from compressively sensed measurements," *In Proc. IEEE Comput. Soc. Conf. Comput. Vis. Pattern Recognit. (CVPR)*, Jun. 2016.
- [23] W. Shi, F. Jiang, S. Liu, and D. Zhao, "Multi-scale deep networks for image compressed sensing," *In Proc. IEEE Int. Conf. on Image Process. (ICIP)*, Oct. 2018.
- [24] H. Yao, F. Dai, S. Zhang, Y. Zhang, Q. Tian, and C. Xu, "Dr²-net: Deep residual reconstruction network for image compressive sensing," *Neurocomputing*, vol. 359, pp. 483–493, Sep. 2019.
- [25] R. Liu, S. Li, , and C. Hou, "An end-to-end multi-scale residual reconstruction network for image compressive sensing," *In Proc. IEEE Int. Conf. on Image Process. (ICIP)*, Sep. 2019.
- [26] W. Shi, F. Jiang, S. Liu, and D. Zhao, "Image compressed sensing using convolutional neural network," *IEEE Trans. Image Process.*, vol. 29, pp. 375–388, Jul. 2019.
- [27] W. Shi, F. Jiang, S. Liu, and D. Zhao, "Scalable convolutional neural network for image compressed sensing," *In Proc. IEEE Comput. Soc. Conf. Comput. Vis. Pattern Recognit. (CVPR)*, Jun. 2019.
- [28] J. Zhang and B. Ghanem, "Ista-net: Interpretable optimization-inspired deep network for image compressive sensing," *In Proc. IEEE Comput. Soc. Conf. Comput. Vis. Pattern Recognit. (CVPR)*, Jun. 2018.
- [29] Pavan Kumar Reddy K. and K. N. Chaudhury, "Learning iteration-dependent denoisers for model-consistent

compressive sensing,” *In Proc. IEEE Int. Conf. on Image Process. (ICIP)*, Sep. 2019.

- [30] Amir. Beck, *First-Order Methods in Optimization*, MOS-SIAM Ser. Optim., 2017.
- [31] C. Dong, C. C. Loy, K. He, and X. Tang, “Learning a deep convolutional network for image super-resolution,” *In Proc. Eur. Conf. Comput. Vis. (ECCV)*, pp. 184–199, 2014.
- [32] K. Hornik, M. Stinchcombe, and H. White, “Multi-layer feedforward networks are universal approximators,” *Neural Networks*, vol. 2, no. 5, pp. 359–366, 1989.
- [33] J. Liu, X. Chen, Z. Wang, and W. Yin, “ALISTA: Analytic weights are as good as learned weights in LISTA,” *In Proc. Int. Conf. Learning Representations (ICLR)*, May 2019.
- [34] X. Glorot and Y. Bengio, “Learning a deep convolutional network for image super-resolution,” *In Proc. Mach. Learn. Research (PMLR)*, vol. 9, pp. 249–256, 2010.
- [35] A. Adler, D. Boubilil, and M. Zibulevsky, “Block-based compressed sensing of images via deep learning,” *In Proc. IEEE Int. Workshop on Multimedia Signal Process. (MMSPS)*, Oct. 2017.
- [36] K. Zhang, W. Zuo, S. Gu, and L. Zhang, “Learning deep CNN denoiser prior for image restoration,” *In Proc. IEEE Comput. Soc. Conf. Comput. Vis. Pattern Recognit. (CVPR)*, Jul. 2017.